ACS APPLIED MATERIALS & INTERFACES

Research Article

www.acsami.org

The Role of Ionic Electrolytes on Capacitive Performance of ZnO-Reduced Graphene Oxide Nanohybrids with Thermally Tunable Morphologies

Anand Prakash and D. Bahadur*

Department of Metallurgical Engineering and Materials Science, Indian institute of Technology Bombay, Powai, Mumbai 400 076, India

Supporting Information

ABSTRACT: In the present work, the role of the reaction temperatures on the morphologies of zinc oxide-reduced graphene oxide (ZnO−RGO) nanohybrids and their supercapacitive performance in two different aqueous electrolytes (1.0 M KCl and Na_2SO_4) were investigated. The ZnO−RGO nanohybrids were synthesized at two different temperatures (ca. 95 and 145 °C) by solvothermal method and labeled as ZnO−RGO-1 and ZnO−RGO-2, respectively. The structure and composition of ZnO−RGO nanohybrids were confirmed by means of X-ray diffraction, electron microscopes (scanning and transmission), X-ray photoelectron, photoluminescence, and Raman spectroscopy. These results show that the temperature allows a good control on loading and morphology of ZnO nanoassemblies in ZnO−RGO nanohybrids and at elevated temperature of 145 °C, ZnO nanoassemblies break and get completely embedded into RGO matrices. The electrochemical performance of ZnO−RGO nanohybrids was examined by cyclic voltammograms (CVs), galvanostatic charge−discharge (chronopotentiometry) and electrochemical impedance spectroscopy (EIS) in 1.0 M KCl and Na_2SO_4 aqueous electrolytes respectively. Combining the EIS and zeta potential behavior, a direct link between the charge transfer resistance and electrical double layers is established which is responsible for excellent capacitive performance of ZnO−RGO-2. The ZnO−RGO-2 displays high specific capacitance (107.9 F/g, scan rate = 50 mVs^{-1}) in 1.0 M KCl and exhibits merely 4.2% decay in specific capacitance values over 200 cycles.

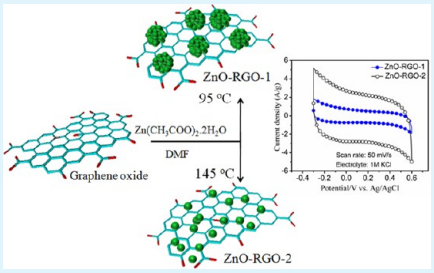

KEYWORDS: *graphene−ZnO nanohybrids, supercapacitor, reduced graphene oxide, energy storage, electrical double-layer capacitors*

1. INTRODUCTION

Electrochemical capacitors, also known as supercapacitors, are considered promising candidates for alternative energy storage devices because of their high rate capability, long cycle life, and low maintenance cost.[1] These are generally categorized into two main types based on their mode of charge-storage mechanisms: (1) electrical double-layer capacitors (EDLCs), where the electrical charges are stored and released by charge separation at the interface between an electrode and an electrolyte; and (2) redox electrochemical capacitors or pseudocapacitors, where capacitance arises from reversible Faradaic reactions and electrosorption at the electrode/electrolyte interface.[2,3] The most commonly investigated nanomaterials used in EDLCs are carbon in its various forms, such as activated carbon, carbon nanotubes, carbon aerogels, xerogels, and hybrid carbon.[3]

Among the diverse types of carbon materials to be used as the electrode of EDLCs, reduced graphene oxide (RGO), which involves oxidation and subsequent reduction of graphite powders,[4,5] holds great promise in supercapacitor applications due to its flexibility, good conductivity, superior chemical stability, large surface-to-volume ratio, tunable pore size distribution, and good corrosion resistance in aqueous electrolyte.[6,7] However, strong van der Waals interaction between their hydrophobic basal planes drives the restacking and aggregation among RGO sheets,[8] and hence limits its application in EDLCs.

Further, the effect of pseudocapacitance for enhancing the total capacitance of graphene materials by quick Faradaic reactions has been realized by insertion of electroactive transition metal oxides such as RuO_2, MnO_2, TiO_2, Fe_3O_4, etc.[9,10] Intercalation of these oxide nanoparticles into the RGO may also prevent the restacking and agglomeration of RGO sheets, which is a major drawback for its use in EDLCs. These transition metal oxides exhibit excellent specific capacitances than EDLCs. However, the phase changes within the electrode due to the faradic reaction results poor lifetime and power density, and thus limits their use as an electrode material. These drawbacks restrict the applications of these oxide materials in graphene based EDLCs and motivate researchers to search for new transition metal oxides.

Hierarchical ZnO nanostructure in particular possesses high specific surface area, environmental compatibility and excellent electrochemical activity, making it a suitable candidate for high

Received: May 24, 2013
Accepted: January 15, 2014
Published: January 15, 2014

performance supercapacitors as compared to other transition metal oxides. Considering this, efforts have been made to structurally integrate ZnO with graphene substrates, leading to hybrid electrodes with improved supercapacitive performance. Recently, Dong et al. has developed a three-dimensional (3D) graphene foam supported ZnO which involves chemical vapor deposition (CVD) growth of graphene followed by in situ precipitation of ZnO nanorods under hydrothermal conditions and investigated its supercapacitive behavior.[11] Lu et al. successfully synthesized graphene/ZnO electrode materials by ultrasonic spray pyrolysis, which exhibited a specific capacitance of 61.7 F/g.[12] Wang et al. has fabricated ZnO−RGO nanohybrids, which showed specific capacitance of 62.2 F/g.[13] Similarly, Chen et al. have synthesized ZnO/reduced graphite oxide composites using a two-step method in which KOH reacts with $Zn(NO_3)_2$ in the aqueous dispersions of graphene oxide (GO) to form a $Zn(OH)_2$/GO precursor, followed by thermal treatment in air.[14] However, most of the synthesis processes discussed above involve two different steps: (1) First, GO is reduced and converted into RGO and then (2) different types of ZnO nanostructures are loaded into RGO sheets by means of various synthesis techniques. Nevertheless, these investigations suggest that ZnO−RGO nanohybrids could possibly be considered as a promising electrode material for supercapacitors. However, despite significant progress, there is a need to address the existing challenges and problems in the field of ZnO−RGO nanohybrids, some of which are listed here: (1) most ZnO−RGO nanohybrids go through a relatively complex two- to three-step synthesis method; (2) poor control on size, surface morphologies, and loading percentage of ZnO nanoparticles on RGO; (3) responses of such nanohybrids toward different type of electrolytes used in supercapacitors. To resolve such issues, herein, we provide an easy one-step solvothermal route for synthesizing ZnO−RGO nanohybrids whose morphologies could be precisely controlled by simply varying the temperature during processing. The two temperatures of 95 and 145 °C were chosen on the basis of certain criterion discussed later in the experimental section. The capacitive behavior of samples was characterized by cyclic voltammetry (CV) and charging-discharging profiles. Further, two commonly used electrolytes in supercapacitors, KCl and Na_2SO_4, with different ionic sizes of cations and anions were used to compare their electrochemical performances.

2. EXPERIMENTAL SECTION

2.1. Materials. Zinc acetate ($Zn(CH_3COO)_2{\cdot}2H_2O$), dimethylformamide (DMF), and potassium hydroxide (KOH) were purchased from Thomas Baker, India. All chemicals were of analytical grade and were used as received. Graphite powder with a particle size of 45 μm (product 496596, 99.99%), hydrazine hydrate (N_2H_4, 80%), H_2SO_4 (98%), HCl (35%), H_2O_2 (30%), and $KMnO_4$ were purchased from Thomas Baker, India, and used without further purification.

2.2. Synthesis of ZnO−RGO Nanohybrids. Graphite oxide was synthesized from graphite powder by a modified Hummers method as described previously.[6] A stable dispersion of graphene oxide (GO) in dimethylformamide (DMF) was prepared by further exfoliation of graphite oxide using ultrasonication and subsequent centrifugation at 5000 rpm (30 min). The ZnO−RGO nanohybrids with different loading capacity of ZnO nanoassemblies were synthesized through a one-step solvothermal route by small variation in processing temperature keeping all other parameters same. The two processing temperatures of 95 and 145 °C were used considering the following logic: It is known[5] that GO starts losing its oxygen function groups (e.g., hydroxyl, epoxide, carbonyl, and carboxyl groups) and reduces to RGO at temperatures above 90 °C. This was the deciding factor for choosing the first temperature of reaction of 95 °C. The higher temperature of 145 °C was selected on the basis of the fact that the boiling point of dimethylformamide is ∼154 °C. Further, the samples were synthesized through the solvothermal method, which puts an obvious upper limit, and therefore 145 °C was a moderate choice for the second reaction temperature.

In a typical protocol, 230.0 mg of zinc acetate ($Zn(CH_3COO)_2{\cdot}2H_2O$) was mixed with 50 mL of suspension of GO. The as-obtained mixture was transferred into a round-bottom flask and refluxed at 95 °C for 6 h. The resulted off white precipitate was washed several times with methanol followed by miliQ water. The final product was dried at 80 °C for 2h and referred as ZnO−RGO-1 in the text. Keeping in mind that the reflux temperature has enormous effect on the growth mechanism of ZnO nanomaterials,[15] we have synthesized another ZnO−RGO nanohybrids at 145 °C, keeping all other parameters same and this is referred as ZnO−RGO-2. For comparison, ZnO nanoassemblies were prepared without GO keeping all other parameters same.

2.3. Characterization. The crystallographic structures and phase confirmation of ZnO−RGO nanohybrids were analyzed by X-ray diffraction (XRD, Philips powder diffractometer PW3040/60 with Cu Kα radiation) and compared with pristine ZnO nanoassemblies. The morphologies and selected area electron diffraction (SAED) patterns were recorded by field-emission transmission electron microscopy (FEG-TEM) using a JEOL JEM-2100 facility. Raman spectra were recorded for these nanohybrids on Lab RAM HR 800 micro-Raman spectroscopy using a 514.5 nm argon laser to confirm the formation of RGO in nanohybrids. Background subtraction was done for the Raman spectra. For X-ray photoelectron spectroscopy (XPS) measurements, samples were drop coated on copper substrate and the analysis was performed using an ESCA probe (MULTILAB from Thermo VG Scientific) with monochromatic Al Kα radiation (energy = 1486.6 eV). The specific surface area, pore volume and pore size distribution of the nanohybrids were measured by ASAP 2020 Micromeritics instrument. Specific surface areas were determined by the multipoint Brunauer−Emmet−Teller (BET) method. The pore size distribution and total pore volume were determined via Brunauer Joyner−Hallenda (BJH) method applied to the desorption branch of isotherms. Prior to analysis, the samples were prepared by degassing at 80 °C for 8 h. The capacitive behavior of nanohybrids were studied in a 3 electrode single-cell system at ambient temperature, with 1.0 M KCl and 1.0 M Na_2SO_4 as the electrolyte solution. Glassy carbon electrode (GCE, diameter Φ = 2 mm), Pt-wire and Ag/AgCl electrodes were used as working, counter and reference electrodes, respectively with electrochemical workstation (CHI660D, Austin, TX). Initially, 200 cycles were performed to stabilize the performance of capacitance for each nanohybrid and its individual components. The electron paramagnetic resonance (EPR) measurements were carried out at X-band on a commercial JEOL spectrometer (JES - FA200). Photoluminescence (PL) measurements of samples were carried using Varian Cary Eclipse.

3. RESULTS AND DISCUSSION

3.1. Structural Analysis. XRD was employed to identify the phases for the as-prepared ZnO−RGO nanohybrids, ZnO and graphite oxide (Figure 1). The XRD pattern of graphite oxide has a sharp peak centered at 2θ = 10.5°, corresponding to an interlayer spacing of 7.88 Å (d_{002}) among stacked GO sheets. This interlayer spacing is much larger than graphite powder (ca. 3.4 Å, before oxidative treatments) owing to the incorporation of various oxygen-containing functional groups (C-Ox) in the sp^3 state and intercalated H_2O molecules in between GO sheets.[5] The diffraction peaks observed in case of both ZnO−RGO nanohybrids (Figure 1c, d) are similar to those of hexagonal wurtzite ZnO (standard X'pert card, Reference pattern 01−075−0576, Figure 1b) as reported earlier in ZnO−RGO nanohybrids.[16,17] However, the diffraction pattern of ZnO−RGO-2 also exhibits a broad hump

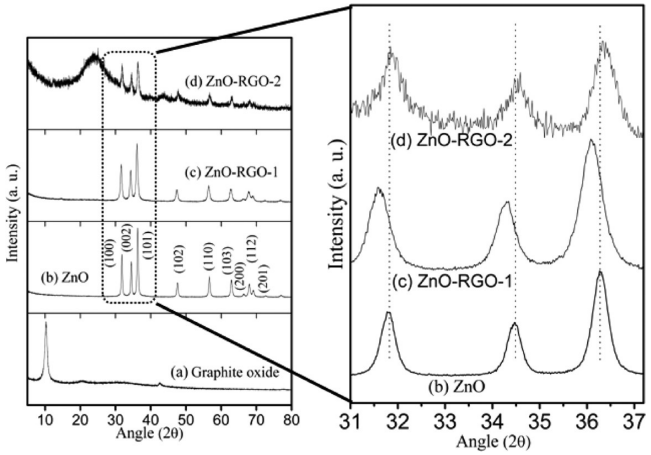

Figure 1. XRD patterns of (a) graphite oxide, (b) ZnO, (c) ZnO−RGO-1, and (d) ZnO−RGO-2. A part of the XRD patterns are highlighted by broken rectangle and the magnified view is located at right.

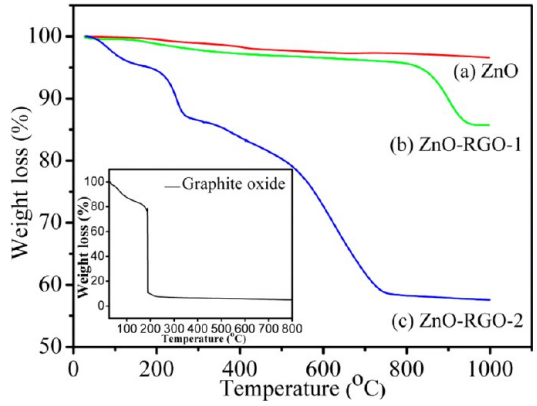

Figure 2. TGA curves of (a) ZnO, (b) ZnO−RGO-1, (c) ZnO−RGO-2, and (inset) graphite oxide.

centered in between 24 and 25°, corresponding to the (002) peak of RGO and is completely missing in ZnO−RGO-1.[18,19] To further investigate the interaction between ZnO and RGO, the rectangular dotted area marked in Figure 1 is magnified (Figure 1, right). The diffraction peaks of the ZnO−RGO-1 are shifted to lower 2θ values compared with that of pristine ZnO (Figure 1b, right), whereas these peaks are unaffected in the case of ZnO−RGO-2. These peak shifts in XRD patterns may be due to deformation of the ZnO lattice because of RGO and may be a measure of interaction between the RGO and ZnO nanoparticles.

In ZnO−RGO-1, the ZnO nanoassemblies (size ∼300−400 nm) are mostly available at the surface of RGO presumably interacting with different functional groups/dangling bonds available on RGO surface, giving rise to shift in d values. However, these nanoassemblies break in to NPs of size ∼30−60 nm at higher temperature and get embedded deep in to RGO to form ZnO−RGO-2. For this, there will be substantial reduction in availability of functional groups/dangling bonds and hence no shift in peaks is expected. Apart from XRD, the distinct features of ZnO−RGO-1 and ZnO−RGO-2 are also supported by electron paramagnetic resonance (EPR, see Figure S5 in the Supporting Information) and photoluminescence (PL) spectra discussed later in the report. Further, these alterations in microstructures are expected in the TEM micrographs discussed later and may have strong influence on capacitive responses of nanohybrids. Also, the (001) diffraction peak of GO absent in ZnO−RGO nanohybrids, may indicate that the regular stacked structure of GO has been prevented because of growth of ZnO nanoassemblies on RGO sheets.[6,20]

Since the ZnO−RGO nanohybrids are synthesized at two different temperatures and it exhibits significant effects on structures of nanohybrids, we anticipate that thermogravimetric analysis (TGA, weight loss profiles) in an inert atmosphere (N_2) may excavate some more information about loading percentage of ZnO in ZnO−RGO nanohybrids. TGA curves of ZnO−RGO-1, ZnO−RGO-2, ZnO and GO are shown in Figure 2. Generally, graphite oxide shows a prominent weight loss at ca. 190−210 °C and is due to loss of chemically bonded oxygen containing functional groups and loss of water molecules in the form of CO, CO_2 and steam as reported earlier.[3,21] In contrast, ZnO nano clusters show a minimal weight loss of only 3% in temperature range of 50−1000 °C, which may be ascribed to the removal of absorbed water and moisture content.[22] Both ZnO−RGO-1 and ZnO−RGO-2 show continuous weight loss but weight loss profile is exorbitant in the case of later one. As shown in Figure 2, the TGA analysis indicates ca. 38.9% RGO content in ZnO−RGO-2, which is more than RGO content in ZnO−RGO-1 (ca. 10.8%). These observations incite us to assume that RGO sheets are not uniformly covered with ZnO nanoassemblies in the case of ZnO−RGO-2.[23] This assumption is further supported by SEM and TEM observations as well as Raman, UV, PL, and XPS spectra and will be discussed later.

Figure 3 shows the Raman spectra of GO, ZnO−RGO-1, and ZnO−RGO-2. The spectrum of GO exhibits two prominent peaks at ∼1592.0 and ∼1353.6 cm^{-1}, which are assigned to the G and D bands, respectively. These bands referred as Raman active E_{2g} phonon (in-plane bond-stretching motion of sp^2 carbon atoms) close to the Γ-point and the breathing mode of k-point phonons of A_{1g} symmetry near the edges of graphitic structures (local defects or disorder).[24,25] The synthesis of ZnO−RGO at two different temperatures involves significant structural changes in carbon framework of GO. Such structural changes can easily be noticed in terms of shift and intensity ratio (I_D/I_G) of D and G bands when compared with GO.[20] For both the ZnO−RGO nanohybrids, the G band shifts to lower wavenumber as compared to pristine GO and are in 1583−1588 cm^{-1} range, indicating the reduction of GO to RGO.[26] Further, ZnO−RGO-1 shows an increased intensity ratio of the D and G bands ($I_D/I_G \approx 1.04$) as compared to that of pristine GO ($I_D/I_G \approx 0.84$), suggesting a decrease in the average size of the sp^2 domains upon the reduction of GO to RGO.[27] This minimization of sp^2 mats of RGO is more prominent in case of ZnO−RGO-2 witnessed in terms of higher I_D/I_G (∼1.16) as compared to I_D/I_G in ZnO−RGO-1. The Raman spectrum of pristine ZnO exhibits a sharp peak at 437.4 cm^{-1} (Figure 3b) corresponding to nonpolar E_2 (high) mode at higher frequencies linked to oxygen deficiency in ZnO nanocrystals.[16] A part of the spectrum of ZnO−RGO-1 and ZnO−RGO-2 in the range of 350−550 cm^{-1} is magnified to visualize the effect of microstructures on the E_2 (high) mode of ZnO and is shown in Figure 3B. It exhibits the characteristic E_2 (high) mode of the ZnO in ZnO−RGO-1 at slightly lower frequency (436.2 cm^{-1}) compared to pristine ZnO and is completely inhibited in ZnO−RGO-2. This again confirms that ZnO NPs are deeply

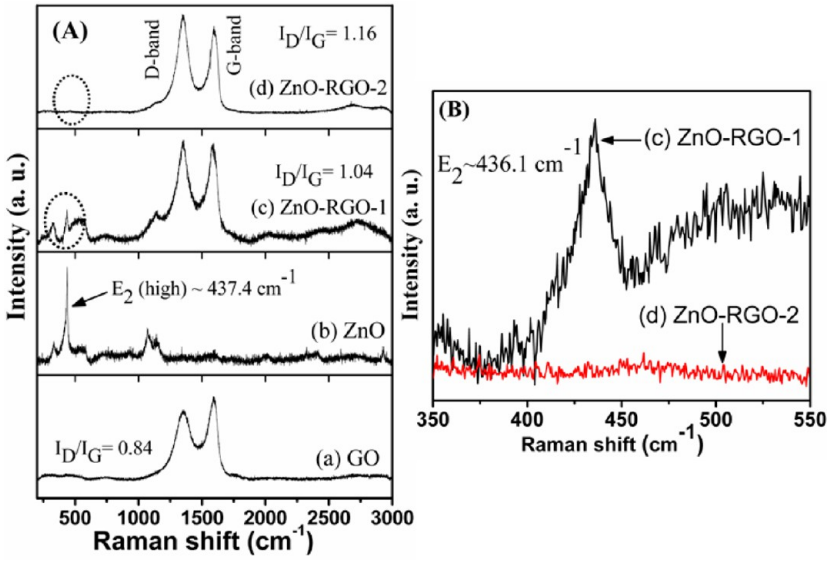

Figure 3. (A) Raman spectra of (a) GO, (b) pristine ZnO NPs, (c) ZnO−RGO-1, and (d) ZnO−RGO-2 nanohybrids. (B) A magnified part of the spectra of ZnO−RGO-1 and ZnO−RGO-2 (elongated circle).

embedded into the RGO sheets and strengthens our belief about distinction between ZnO−RGO-1 and ZnO−RGO-2.

Because both ZnO and GO[28] are UV active, UV−vis absorption spectra exhibit effect of ZnO on the level of electronic conjugation and $\pi \rightarrow \pi^*$ transition in sp^2 network of GO sheets in ZnO−RGO nanohybrids. The spectrum of GO exhibits strong absorption peak at 233 nm (Figure 4), which is

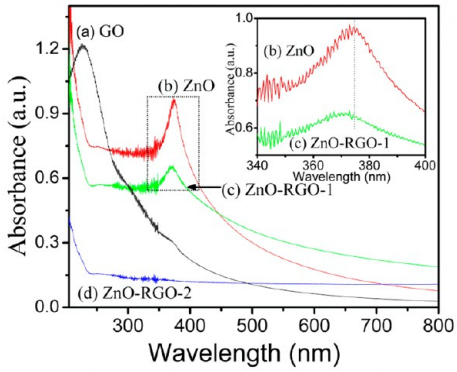

Figure 4. UV−visible absorbance spectra of (a) GO, (b) ZnO, (c) ZnO−RGO-1, and (d) ZnO−RGO-2. The inset shows the amplificatory absorption spectra in the range of 340−400 nm and demarcates the blue shift of ZnO−RGO-1.

due to the $\pi \rightarrow \pi^*$ transition for the C═C bonding as previously reported in case of GO.[29,8] The ZnO−RGO-1 exhibits the blue-shift of UV absorbance band (370 nm) as compared to the ZnO nano clusters (374 nm)[30] whereas the characteristic $\pi \rightarrow \pi^*$ transition peak of GO is completely missing (Figure 4a) suggesting chemical interactions between GO and ZnO nanoparticles.[31,32] Similar blue shift in ZnO−RGO nanohybrids has been reported earlier,[31−33] which suggests that because of the difference in work function of RGO and ZnO while ZnO−RGO nanohybrids are formed, the excess π-electrons of RGO sheets may diffuse toward the ZnO and accumulate at the interface between the RGO and ZnO to form a potential barrier. In contrast, both the UV absorbance features of ZnO and RGO are missing in ZnO−RGO-2 (Figure 4d). These observations might suggest that ZnO nanocrystals are deeply embedded into RGO matrices and show low ZnO content in ZnO−RGO-2. Such assumptions are further supported by SEM microstructures of these nanohybrids. Figure 5a-d shows SEM images of GO, ZnO, and ZnO−RGO nanohybrids. The RGO sheets are wrinkled and corrugated (Figure 5a) whereas ZnO nanoclusters are uniform in shape having diameters 300−400 nm (Figure 5b). These nanoclusters are self-assembly of very tiny ZnO nanoparticles of size 30−60 nm (see Figure S1b in the Supporting Information). In the case of ZnO−RGO-1, ZnO nanoclusters are decorated on RGO sheets and to some extent embedded into the RGO matrices (Figure 5c). In contrast, ZnO nanoclusters break down at higher temperature and are easily embedded into the RGO matrices and are not encountered anywhere on the surface of RGO sheets as seen in ZnO−RGO-2 (Figure 5d). These observations are vivid in the corresponding TEM microstructure as shown in the inset of Figures 5d, which fortify our thought that the ZnO nanoclusters break at higher temperature as discussed above.

Further, to verify complete embedment of ZnO in ZnO−RGO-2, photoluminescence (PL) spectra were recorded for the samples (Figure 6). Both ZnO and ZnO−RGO-1 exhibit a strong excitonic emission peak centered at ~380 nm and a broad defect-related green emission (DRGM) hump ranging in between 500 and 700 nm. The excitonic peak is a well-known signature of radiative recombination of electrons from conduction band with holes from valence band whereas the DRGM is generally attributed to the recombination of electrons trapped in V_{oS}^{+} (surface defects) with photo excited holes.[34] It is striking that the excitonic emission peak (~380 nm) is entirely absent in case of ZnO−RGO-2. Further, we have compiled the DRGM of all samples on one platform along with their counts in the inset of Figure 6 to see how DRGM of ZnO responds in ZnO−RGO-1 and ZnO−RGO-2. A reason of interest of DRGM profiles of nanohybrids is magnified (broken rectangle), which clearly indicates that there is a sudden drop in DRGM profile of ZnO−RGO-1 followed by complete inhibition in case of ZnO−RGO-2 justifying embedment of ZnO in ZnO−RGO-

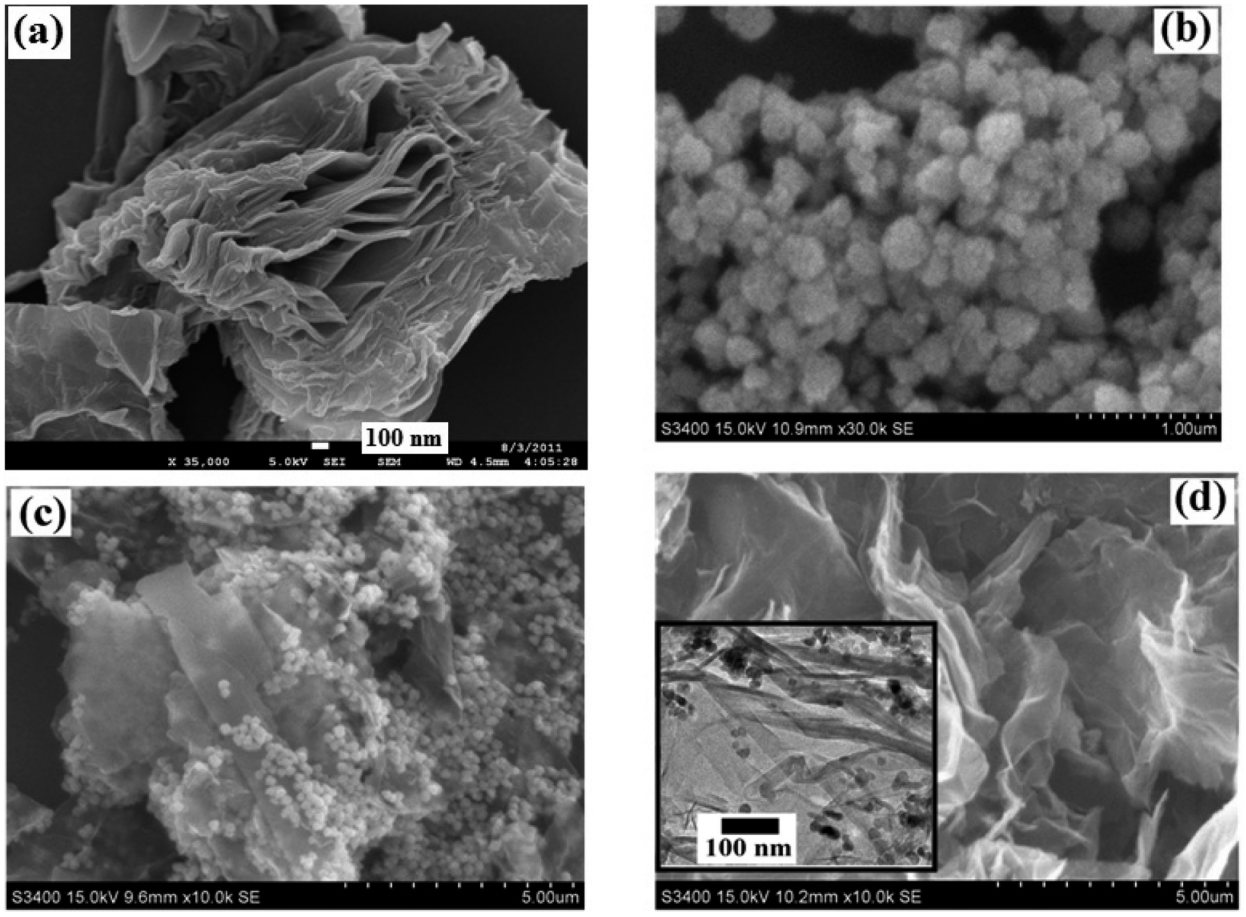

Figure 5. SEM micrographs of (a) GO, (b) ZnO nanoclusters, (c) ZnO−RGO-1, and (d) ZnO−RGO-2. The inset of d shows the corresponding TEM microstructure of ZnO−RGO-2. The corresponding TEM microstructures of GO, ZnO ,and ZnO−RGO-1 are given in the Supporting Information (Figure S1).

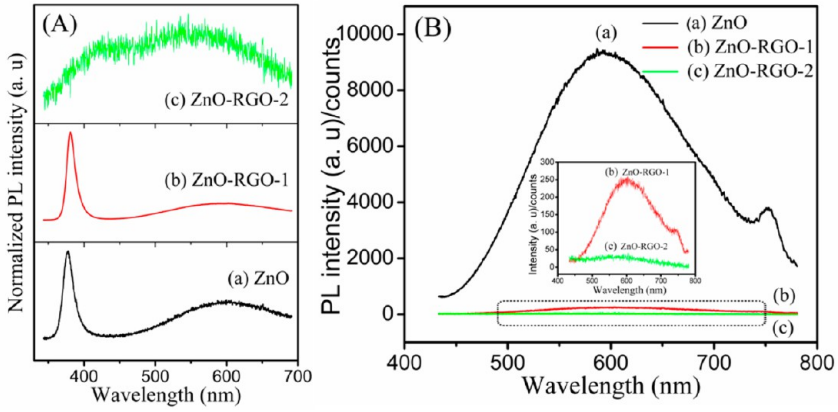

Figure 6. (A) PL spectra with normalized intensity for (a) ZnO, (b) ZnO−RGO-1, and (c) ZnO−RGO −2. (B) Defect band emission spectra are put together to show that defect emission is completely inhibited in ZnO−RGO-2. For realization, we are showing the counts at *y*-axis.

2. Quenching of DRGM because of ZnO in ZnO−RGO nanohybrids is well-established and provides a facile method to monitor the interfacial electron-transfer processes.[29] However, we propose that this interfacial electron-transfer is more pronounced when ZnO nanoassemblies are broken and are embedded in to RGO matrices as clearly indicated by the PL spectra of ZnO−RGO-2 (Figure 6Bb, c). In ZnO−RGO-2, ZnO is present in the form of single particle entities of much smaller dimension (∼30−60 nm), unlike nanoassemblies (300−400 nm), which leads to enhancement of the contact area between ZnO and RGO due to smaller size of ZnO NPs as compared to ZnO nanoassemblies. This further strengthens the ability of transfer of photogenerated electrons to carbon materials, and thus the DRGM is completely diminished.

We further investigate the chemical interaction between ZnO nanoassemblies and RGO sheets, degree of GO reduction, and chemical states of C1s and O1s by X-ray photoelectron spectroscopy (XPS). The survey spectra of ZnO−RGO

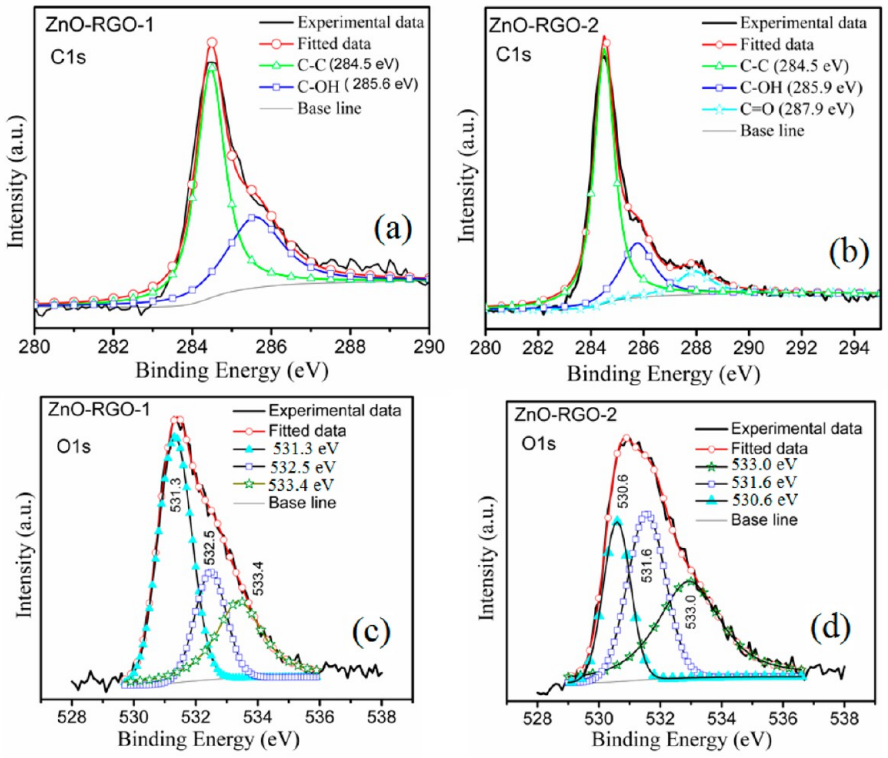

Figure 7. XPS spectra of ZnO−RGO-1 and ZnO−RGO-2. (a, b) deconvoluted C1s spectra of ZnO−RGO-1 and ZnO−RGO-2. (c, d) deconvoluted O1s spectra of ZnO−RGO-1 and ZnO−RGO −2 in three different components.

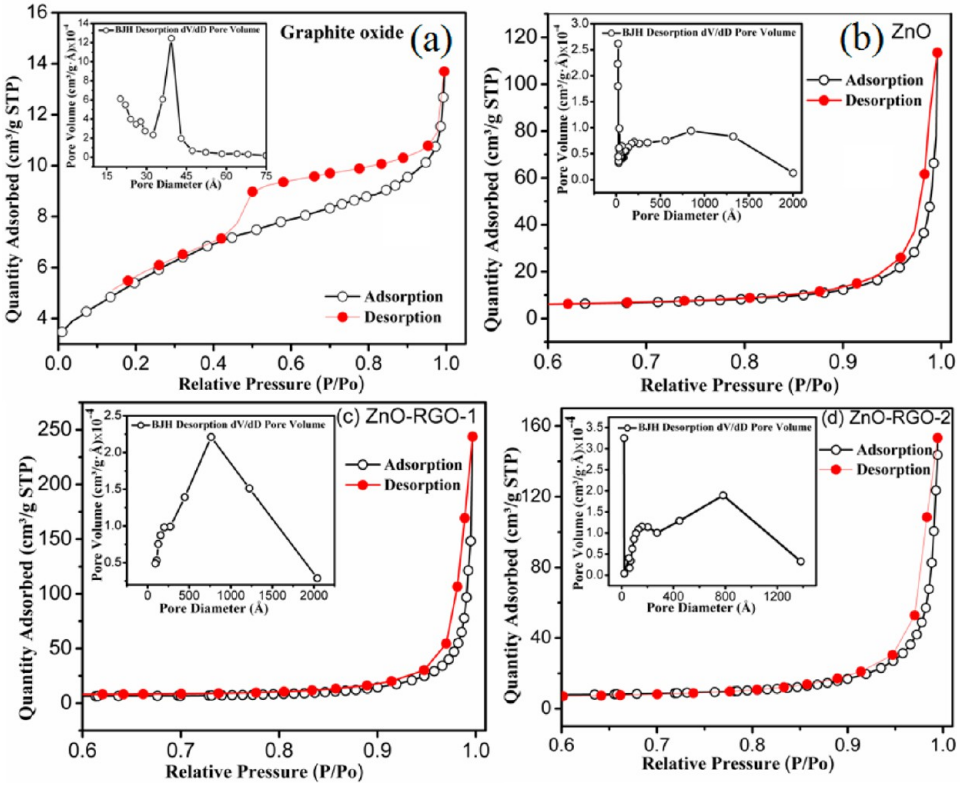

Figure 8. Nitrogen adsorption/desorption isotherm and pore size distribution (inset) of the as prepared nanohybrids (a) GO, (b) ZnO, (c) ZnO−RGO-1, and (d) ZnO−RGO-2. The filled and open symbols indicate adsorption and desorption branches.

nanohybrids between 200 and 1200 eV bring out the characteristic peaks of $Zn2p_{1/2}$, $Zn2p_{3/2}$, O1s, and C1s only (see Figure S2a in the Supporting Information) and further rule out the existence of any phase or contamination during the growth of ZnO nanoassemblies on RGO sheets. Figure S2b in the Supporting Information shows high-resolution XPS peaks

dx.doi.org/10.1021/am405031y | ACS Appl. Mater. Interfaces 2014, 6, 1394−1405

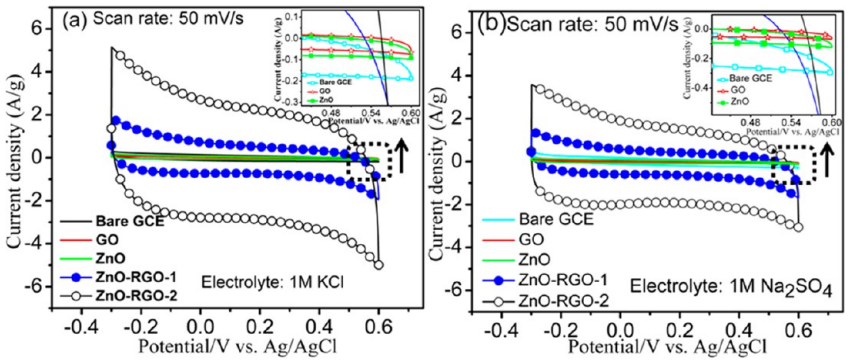

Figure 9. (a) Cyclic voltammograms of bare GCE, GO, ZnO, ZnO−RGO-1, and ZnO−RGO-2 nanohybrids at a voltage scan rate of 50 mV/s in different electrolytes: (a) 1.0 M KCl and (b) 1.0 M Na_2SO_4. Insets show zoom-in CV responses of bare GCE, GO, and ZnO.

of Zn (2p) core level of ZnO−RGO-1 and ZnO−RGO-2 respectively. The ZnO−RGO-1 shows doublet spectral lines at 1022 eV ($Zn2p_{3/2}$) and 1045 eV ($Zn2p_{1/2}$) with a spin−orbit splitting (ΔE) of 23.0 eV. In contrast, the peak positions of doublet spectral lines (Zn2P) of ZnO−RGO-2 are slightly switched to lower binding energies with a slightly higher spin−orbit splitting (ΔE) of 23.4 eV. The deconvoluted C1s and O1s XPS spectra of ZnO−RGO nanohybrids deposited on the cleaned silicon substrate have been shown in Figure 7a−d. In ZnO−RGO-1, the C1s spectrum is deconvoluted in two different peaks centered at 284.5 eV(C═C) and 285.6 eV (C−OH), respectively. In contrast, it is deconvoluted into three different peaks centered at 285.5 eV (C═C), 285.9 eV (C−OH), and 287.9 eV (C═O) in case of ZnO−RGO-2. These spectra reveal that the intensities of the bands corresponding to carboxyl, epoxide, and hydroxyl functional groups are greatly reduced and attributed to the fact that a large amount of surface oxide groups of GO is chemically reduced during synthesis of ZnO−RGO nanohybrids.[35] In our earlier work, it was suggested that the deconvoluted O1s spectra of ZnO−RGO assemblies might reveal information about the stability and chemical environment around ZnO of such nanohybrids.[16] Further, it has been reported that oxygen contribution coming from ZnO may effectively shift the peak position of O1s in such systems.[36] Thus, a typical O1s peak of ZnO−RGO-1 is deconvoluted into three Gaussian peaks, which center at 529.8, 530.5, and 531.9 eV. The higher binding energy peaks located at 531.9 and 530.5 eV are assigned to loosely bound oxygen (from sources such as adsorbed H_2O or O_2) on the surface of the ZnO nanocrystals, whereas the lower binding energy of 529.8 eV is attributed to the O^{2-} ion (Zn−O bonding) in the wurtzite structure of hexagonal ZnO.[37] The O1s core-level peak (Figure 7d) of ZnO−RGO-2 can also be resolved into three components centered at 530.4, 531.0, and 532.0 eV by a Gaussian function with a slightly lower energy as compared to ZnO−RGO-1. These observations strengthen our belief that ZnO nanoclusters are deeply embedded into RGO matrices and allow minimal oxygen contribution from ZnO in O1s spectra of ZnO−RGO-2. Importantly, the ratio of intensities of the middle and higher binding energy peaks follows the same profile (Middle one is higher than higher binding energy peaks) in both ZnO−RGO-1 and ZnO−RGO-2, whereas the intensity ratios of the peak with the lower binding energy to middle one is higher than ZnO−RGO-2. This shows that reaction temperature may profoundly change the chemical states of O1s in ZnO−RGO nanohybrids.

The N_2 adsorption−desorption isotherms were recorded to investigate the porous structure and surface area of ZnO, GO and ZnO−RGO nanohybrids as shown in Figure 8a−d. The isotherms for ZnO, ZnO−RGO-1, and ZnO−RGO-2 exhibit hysteresis, which are parallel to *y*-axis. These isotherms are classified as type IV, which characterizes mesoporous solids, according to IUPAC classification.[6,38] However, the isotherm of graphite oxide also shows typical type IV behavior but with a hysteresis loop parallel to *x*-axis. This signifies that the nature of pores in graphite oxide is entirely different from ZnO and ZnO−RGO nanohybrids. The distribution of pores is broad in case of ZnO, ZnO−RGO-1 and ZnO−RGO-2 (insets of Figure 8b−d). In contrast, graphite oxide exhibits very narrow pore size distribution (inset of Figure 8a). The textural properties of nanohybrids along with ZnO and GO are listed in Table S1 in the Supporting Information. The nature of hysteresis of nanohybrids are type H-3 according to IUPAC classification[38,39] and this signifies to the capillary condensation of N_2 in slit-shaped pores developed due to folded RGO sheets and their attachments to ZnO nanoclusters. This means that graphite oxide does not change the type of pores in ZnO−RGO nanohybrids even though these were synthesized at different temperatures. It is worth noting that the surface area of ZnO−RGO-2 is higher than ZnO−RGO-1 because ZnO nanoparticles are completely embedded in the RGO sheets (Figure 8d) and can act as spacers between RGO sheets, thereby preventing their agglomeration.

3.2. Electrochemical Studies for Capacitance Measurement. The electrochemical studies were performed in a three electrode glass cell geometry to analyze the capacitive behavior of GO, ZnO, ZnO−RGO-1 and ZnO−RGO-2 nanohybrids respectively (Figure 9a) where a 1.0 M KCl was used as an electrolyte. The CV curves of both ZnO−RGO nanohybrids exhibit nearly rectangular shape and symmetry at a voltage sweep rate of 50 mV/s. This indicates a good charge propagation at the electrode surface, possession of an electrical double layer (EDL) and a low contact resistance in the electrode.[40,41] The specific capacitance of the nanohybrids are calculated from CV curves according to the following equation[42]

$$C_{sp}\ (\mathrm{F/g}) = \frac{1}{2mv(v2 - v1)} \int_{v1}^{v2} I(v)\mathrm{d}v \qquad (1)$$

where m is the mass of single electrode material, v is the scan rate (mV/s), $v1$ and $v2$ are the integration limits (potential window), and $I(v)$ denotes the response current (A). The specific capacitances of ZnO−RGO-1 calculated from CV curve

Table 1. Specific Capacitances of Nanohybrids at Different Scan Rates in 1.0 M KCl as an Electrolyte

	specific capacitance (F/G) (electrolyte, 1.0 M KCl)				
sample	voltage scan rate (50 mV/S)	voltage scan rate (100 mV/S)	voltage scan rate (200 mV/S)	voltage scan rate (500 mV/S)	voltage scan rate (1000 mV/S)
GO	1.6	1.4	1.3	1.2	1.1
ZnO	2.6	2.3	2.0	1.7	1.5
ZnO−RGO-1	29.8	25.7	22.7	19.5	17.2
ZnO−RGO-2	107.3	94.1	81.8	66.0	53.5

Table 2. Specific Capacitances of Nanohybrids at Different Scan Rates in an Electrolyte 1.0 M Na_2SO_4

	specific capacitance (F/g) (electrolyte, 1.0 M Na_2SO_4)				
sample	voltage scan rate (50 mV/s)	voltage scan rate (100 mV/s)	voltage scan rate (200 mV/s)	voltage scan rate (500 mV/s)	voltage scan rate (1000 mV/s)
GO	1.4	1.1	0.9	0.8	0.7
ZnO	2.4	2.2	1.8	1.4	1.5
ZnO−RGO-1	24.6	20.8	17.8	14.5	12.4
ZnO−RGO-2	74.8	67.9	62.0	55.3	49.5

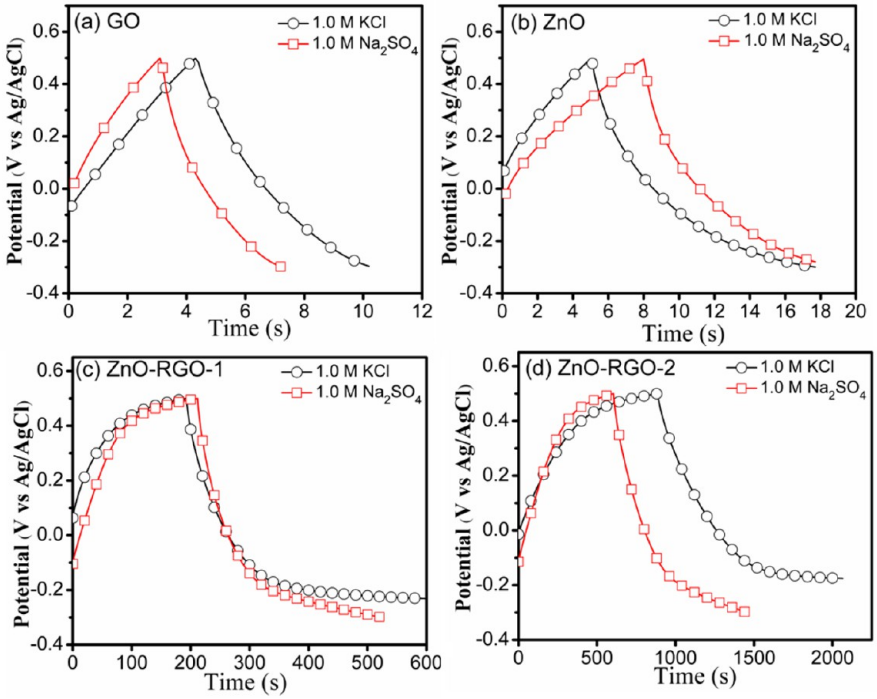

Figure 10. Galvanostatic charge/discharge profiles of (a) GO, (b) ZnO, (c) ZnO−RGO-1, and (d) ZnO−RGO-2, respectively, in two different electrolytes (1.0 M KCl and Na_2SO_4) at constant current density of 0.1 A/g.

at a scan rate of 50 mV/s is 29.8 F/g. In contrast, the measured specific capacitance of ZnO−RGO-2 is 107.3 F/g, which is three times higher than ZnO−RGO-1(Figure 9a Table 1). This may be attributed to the fact that ZnO is comp0letely embedded in to RGO matrices in case of ZnO−RGO-2, which greatly improves the double-layer capacitance of the nanohybrids by forming a porous structure having high specific surface area.

In addition, the effect of different voltage sweep rates (50, 100, 200, 500, and 1000 mV/s) on the specific capacitance was examined for ZnO−RGO nanohybrids along with ZnO and GO in 1.0 M KCl and Na_2SO_4, respectively (Tables 1 and 2). It is shown that successive increment in voltage sweep rate results continuous loss in capacitance for each sample, attributing to the fact that under higher scan rates, the active material is not fully utilized because of the concentration polarization, which slows down the diffusion rates of electrolyte ions.[7] In this context, to explore the influence of electrolyte type on the performance of a supercapacitor, typical CV curves of samples at different voltage scan rates were also recorded in 1.0 M Na_2SO_4 and are displayed in Figure 9b. Here also, we have observed fairly rectangular CV curves, indicating good charge propagation and the possession of stable EDL at the electrode surfaces even after switching electrolytes from KCl to Na_2SO_4. However, it is noteworthy that by exchanging electrolytes from KCl to Na_2SO_4, each nanohybrid exhibits a significant reduction in specific capacitance, but the line profile remains essentially the same (Figure 9b), indicating that the fundamental charge-transfer mechanism has not been changed. To obtain more information about the nanohybrids as electrode materials for supercapacitors, galvanostatic charge/discharge measurements were carried out in both 1.0 M

dx.doi.org/10.1021/am405031y | ACS Appl. Mater. Interfaces 2014, 6, 1394−1405

Na_2SO_4 and KCl separately between −0.3 and 0.5 V at a current density of 0.1 A/g (Figure 10a–d). Panels c and d in Figure 10 indicate that the discharge time for ZnO–RGO-2 is higher than that for ZnO–RGO-1 in both the electrolytes, which is an indication of higher specific capacitance for ZnO–RGO-2. The specific capacitance determined from galvanostatic charge/discharge is calculated by using the formula C_{sp} (F/g) = $I/m(dV/dt)$, where m is the mass of the electrode material and (dV/dt) is being taken from the upper half of the discharge curve after the IR drop as a convention.[43] Table 3 lists the value of specific capacitance in 1.0 M KCl and Na_2SO_4 respectively. The galvanostatic charge/discharge also indicates that specific capacitance of ZnO–RGO-2 is higher than ZnO–RGO-1 in both the electrolytes. Thus, both CVs and galvanostatic charge/discharge profiles together attribute to the fact that capacitive performance is better in KCl than Na_2SO_4 and that may be due to more access of K^+ ions toward available pores or voids of the nanohybrids as compared to Na^+ ions.

Table 3. Specific Capacitances of Nanohybrids at Constant Current Density (0.1 A/g) in 1.0 M KCl and Na_2SO_4, Respectively

	specific capacitance (F/g) at current density 0.1 A/g (galvanostatic)	
sample	1.0 M KCl	1.0 M Na_2SO_4
GO	0.5	0.3
ZnO	0.7	0.5
ZnO–RGO-1	18.0	12.0
ZnO–RGO-2	83.3	45.8

Because ZnO–RGO-2 gives the highest value of specific capacitance, it is reasonable to ensure about its cyclic stability. Figure 11 displays the specific capacitance of the ZnO–RGO-2 in the range of −0.3–0.5 V as a function of charge–discharge cycle numbers at 1.0 A/g in 1.0 M KCl and Na_2SO_4 aqueous electrolytes, respectively. As illustrated in Figure 11a, ZnO–RGO-2 shows higher value of specific capacitance in KCl as compared to Na_2SO_4 as shown in panels a and b in Figure 9. Further, panels b and c in Figure 11 demonstrate that ZnO–RGO-2 maintains a reasonable level of cyclic stability and reversibility even after 200 cycles by preserving a symmetric charging–discharging shape both in 1.0 M KCl and Na_2SO_4. These results indicate that ZnO embedded in RGO sheets acts as a base material and effectively prevents the morphological changes such as swelling/shrinking and aggregation of electroactive materials during the charging/discharging processes. The ZnO–RGO-2 nanohybrid demonstrates an excellent cyclic stability by sustaining 95.8% and 96.4% of specific capacitance as compared to their initial values in KCl and Na_2SO_4, respectively, over 200 cycles.

A possible explanation reasserting stability of ZnO–RGO nanohybrids is discussed here. In contrast to transition metal oxides[44] such as nickel hydroxide, nickel oxide, cobalt hydroxide, cobalt oxide, manganese oxide, etc., the CV response of pristine ZnO in both the electrolytes (1.0 M KCl and Na_2SO_4) is nearly rectangular even at very high scan rates (see the Supporting Information, Figure S4). This signifies that ZnO does not undergo a very large volume expansion/contraction and the charge storage mechanism is dominated by rapid adsorption/desorption of electrolyte ions. On the other hand, RGO has been widely accepted as a buffer matrix to accommodate volume expansion/contraction in transition metal oxides because of its superior electrical conductivity, excellent mechanical flexibility, and high thermal and chemical stability.[45]

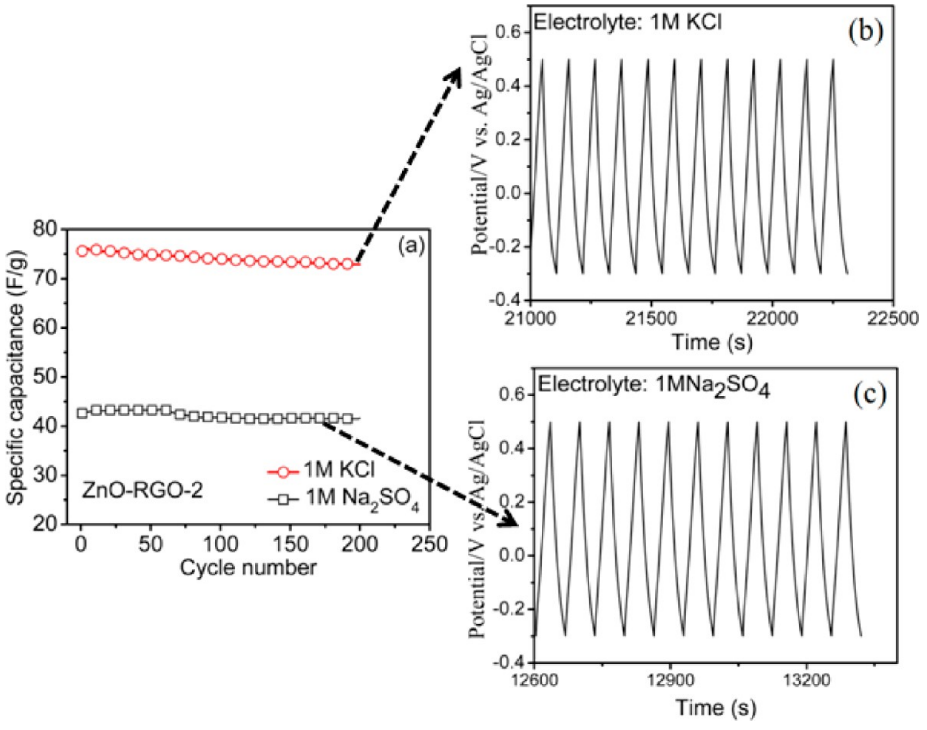

Figure 11. (a) Cycle performance (specific capacitance) of ZnO–RGO-2 nanohybrid electrode at the current density of 1.0 A/g in 1.0 M KCl and Na_2SO_4 electrolytes. (b, c) Galvanostatic charge/discharge profiles of ZnO–RGO-2 in 1.0 M KCl and Na_2SO_4, respectively.

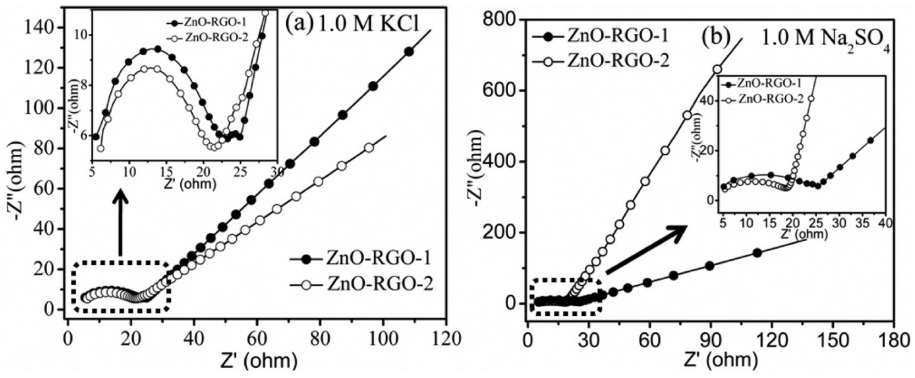

Figure 12. Nyquist plots of nanohybrids ZnO−RGO-1 and ZnO−RGO-2 in different electrolytes: (a) 1.0 M KCl and (b) 1.0 M Na_2SO_4. The high-frequency regions (broken rectangle) are magnified and given in the insets. The morphology has little effect on the ohmic resistance but greatly affects the charge transfer (R_{ct}) and diffusion resistance.

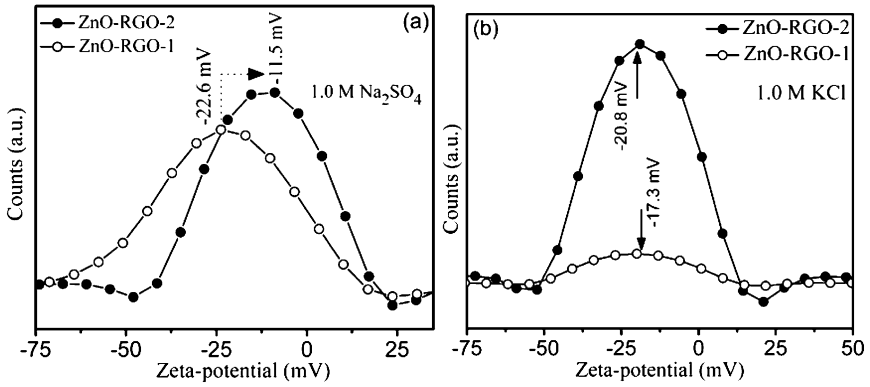

Figure 13. Zeta potentials of colloidal suspension of ZnO−RGO-1 and ZnO−RGO-2 in (a) 1.0 M Na_2SO_4 and (b) 1.0 M KCl.

Thus, both the features of ZnO and RGO are synchronized together to stabilize ZnO−RGO nanohybrids if any volume expansion/contraction persists during electrochemical cycling.

Electrochemical impedance spectroscopy (EIS) has been recognized as one of the principal techniques for examining the electron and ion transport in electrode materials. The EIS spectra (Nyquist plots) of ZnO-RGO nanohybrids were measured in 1.0 M KCl and Na_2SO_4 (frequency range ~0.1 to 1×10^6 Hz) at an open circuit potential and the typical plots for these electrodes consist of a semicircle arc at higher frequencies and a linear straight line at lower frequencies as shown in Figure 12a, b. The diameter of high-frequency semicircle arc represents charge transfer limiting process and is assigned to a combination of Faradic charge transfer resistances (R_{ct}) in parallel with the double-layer capacitances at the interfaces between electrode and electrolyte.[46] The low-frequency straight line- inclining to the real axis corresponds to Warburg impedance. The slope of Warburg impedance decides diffusion of electrolyte ions to the electrodes and a vertical line normal to the real axis corresponds to zero diffusion resistance.[7,47] It has been observed that the semicircle arch originates from the same position in both the electrolytes, which signifies that morphological difference in ZnO−RGO nanohybrids has little effect on the ohmic resistance of the supercapacitor device, as shown in the zoom-in of the rectangle (insets of Figure 12a, b). Further, the R_{ct} values of ZnO−RGO-2 measured in 1.0 M KCl and Na_2SO_4 are 21.2 and 18.5 ohms, respectively, and are lower than ZnO−RGO-1 ($R_{ct(KCl)} \approx 24.8$ ohm and $R_{ct(Na_2SO_4)} \approx 25.8$ ohm). The lower values of R_{ct} attribute to the porous structure of ZnO−RGO-2, facilitating the efficient access of electrolyte ions to the surface of electrode. The diffusion responses of electrolyte ions (low-frequency EIS plots) in ZnO−RGO-1 and ZnO−RGO-2 are contrary to each other. In KCl, the ZnO−RGO-1 makes larger slope to the real axis than ZnO−RGO-2, whereas in Na_2SO_4, the slope profile flips and now the slope of ZnO−RGO-2 to real axis is larger than ZnO−RGO-1. These observations signify that R_{ct} plays a key role and is responsible for superior capacitive behavior of ZnO−RGO-2 in both the electrolytes.

To get a deeper understanding over superior capacitive behavior of ZnO−RGO-2 as compared to ZnO−RGO-1 in both the electrolytes (KCl and Na_2SO_4), the zeta potentials of ZnO−RGO-1 and ZnO−RGO-2 were recorded by dispersing them in aqueous electrolytes having same strength as in case of CV and EIS measurements (1.0 M KCl and Na_2SO_4). These analyses enable us to interpret the nature of electrical double layers (EDL) around the nanohybrids when dispersed in different electrolytes. The zeta potential of ZnO−RGO-1 is negative and higher than that of ZnO−RGO-2 in Na_2SO_4 (Figure 13a). In contrast, the values of zeta potentials of these nanohybrids flip in KCl and now ZnO−RGO-2 indicates slightly higher negative value of zeta potentials than ZnO−RGO-1(Figure 13b). Such contrary features have also been encountered in the low-frequency profiles of EIS spectra (Figure 12a, b). According to the Derjaguin, Landau, Verwey, and Overbeek (DLVO) theory, the thickness of EDL or zeta potential depends on nature of electrolytes and decrease markedly with the ionic concentration.[48] In Na_2SO_4, the EDL in ZnO−RGO-1 is thicker than ZnO−RGO-2, but its specific capacitance is lower than ZnO−RGO-2. This might be possible

because of higher R_{ct} of ZnO−RGO-1 than ZnO−RGO-2. In KCl, ZnO−RGO-2 shows thicker EDL and a lower R_{ct} value than ZnO−RGO-1, thus resulting three times higher specific capacitance than ZnO−RGO-1. Thus, we conclude that both R_{ct} and EDL are important parameters and a thicker EDL and lower value of R_{ct} guarantee the superior capacitive behavior of ZnO−RGO-2. These outcomes exhibit that ZnO−RGO-2-based supercapacitors possess good stability, lifetime and a high degree of reversibility in the repetitive charging-discharging cycle and appears as a potential electrode for supercapacitors.

4. CONCLUSIONS

We have synthesized the ZnO−RGO nanohybrids at two different temperatures (95 and 145 °C). The reaction temperature has enormous effects on the microstructures and loading % of ZnO into ZnO−RGO nanohybrids. In case of ZnO−RGO-1, ZnO nanoassemblies of size 300−400 nm are well-distributed on the RGO sheets. In contrast, in ZnO−RGO-2, these nanoassemblies break at higher temperature and individual ZnO nanoparticles of sizes ∼30−60 nm are embedded completely into RGO sheets. The influence of electrolyte type on the performance of the ZnO−RGO based supercapacitors has been investigated. The ZnO−RGO-2 exhibits superior capacitive behavior than ZnO−RGO-1, particularly in 1.0 M KCl and achieves a specific capacitance as high as 107.0 F/g at a scan rate of 50 mVs^{-1}. The EIS and zeta potential behaviors reveal that a lower R_{ct} value and thicker EDL formations are responsible for its superior capacitive behavior. Furthermore, ZnO−RGO-2 merely shows less than 5% decay in specific capacitance values over 200 cycles at a current density of 1.0 A/g and demonstrates excellent cycling performance in both the electrolytes. These results suggest that electrochemical performance including capacitive performance of nanohybrids depend on microstructures and loading % of ZnO in RGO and a deeper loading of ZnO results improved capacitive performance. The above studies are fundamental and enlighten us on how the microstructures of ZnO−RGO nanohybrids can be thermally tunable, which can strongly influence the electrochemical performance in different electrolytes.

■ ASSOCIATED CONTENT

Supporting Information

TEM microstructures and BET surface area of graphite oxide, ZnO, ZnO−RGO-1, and ZnO−RGO-2 nanohybrids. X-ray photoelectron (XPS) survey spectra of the ZnO−RGO nanohybrids with Zn2p doublet spectral lines. Electron paramagnetic resonance (EPR) spectra of ZnO−RGO nanohybrids. This material is available free of charge via the Internet at http://pubs.acs.org/.

■ AUTHOR INFORMATION

Corresponding Author

* E-mail: dhirenb@iitb.ac.in. Phone: + 91-22-2576 7632. Fax: + 91-22-2582 348.

Notes

The authors declare no competing financial interest.

■ ACKNOWLEDGMENTS

Financial support from Nano mission of the Department of Science and Technology, Government of India, is greatly acknowledged. The authors are grateful to the Centre for Research in Nanotechnology and Central Surface Analytical Facility, IIT Bombay, for TEM and XPS facilities.

■ REFERENCES

(1) Bordjiba, T.; Mohamedi, M.; Dao, L. H. *Adv. Mater.* **2008**, *20*, 815−819.
(2) Pandolfo, A. G.; Hollenkamp, A. F. *J. Power Sources* **2006**, *157*, 11−27.
(3) Frackowiaka, E.; Francois, B. *Carbon* **2001**, *39*, 937−950.
(4) Hummers, W. S.; Offeman, R. E. *J. Am. Chem. Soc.* **1958**, *80*, 1339.
(5) Stankovich, S.; Dikin, D. A.; Piner, R. D.; Kohlhaas, K. A.; Kleinhammes, A.; Jia, Y.; Wu, Y.; Nguyen, S. T.; Ruoff, R. S. *Carbon* **2007**, *45*, 1558−1565.
(6) Prakash, A.; Chandra, S.; Bahadur, D. *Carbon* **2012**, *50*, 4209−4219.
(7) Stoller, M. D.; Park, S.; Zhu, Y.; An, J.; Ruoff, R. S. *Nano Lett.* **2008**, *8* (10), 3498−3502.
(8) Li, D.; Muller, M. B.; Gilje, S.; Kaner, R. B.; Wallace, G. G. *Nat. Nanotechnol.* **2008**, *102*, 101−105.
(9) Mishra, R. K.; Ramaprabhu, S. *J. Phys. Chem. C* **2011**, *115*, 14006−14013.
(10) Ying, Li.; Zhao, N.; Shi, C.; Liu, E.; He, C. *J. Phys. Chem. C* **2012**, *116*, 25226−25232.
(11) Dong, X.; Cao, Y.; Wang, J.; Chan-Park, M. B.; Wang, L.; Huang, W.; Chen, P. *RSC Adv.* **2012**, *2*, 4364−4369.
(12) Lu, T.; Zhang, Y.; Li, H.; Pan, L.; Li, Y.; Sun, Z. *Electrochim. Acta* **2010**, *55*, 4170−4173.
(13) Wang, J.; Gao, Z.; Li, Z.; Wang, B.; Yan, Y.; Liu, Q.; Mann, T.; Zhang, M.; Jiang, Z. *J. Solid State Chem.* **2011**, *184*, 1421−1427.
(14) Chen, Y. L.; Hu, Z. A.; Chang, Y. Q.; Wang, H. W.; Zhang, Z. Y.; Yang, Y. Y.; Wu, H. Y. *J. Phys. Chem. C* **2011**, *115*, 2563−2571.
(15) Xu, X.; Xu, C.; Dai, J.; Hu, J.; Li, F.; Zhang, S. *J. Phys. Chem. C* **2012**, *116*, 8813−8818.
(16) Prakash, A.; Misra, S. K.; Bahadur, D. *Nanotechnology* **2013**, *24*, 095705 (10pp).
(17) Son, D. I.; Kwon, B. W.; Park, D. H.; Seo, W. S.; Yi, Y.; Angadi, B.; Lee, C. L.; Choi, W. K. *Nat. Nanotechnol.* **2012**, *7*, 465−471.
(18) Fu, D.; Han, G.; Chang, Y.; Dong, J. *Mater. Chem. Phys.* **2012**, *132*, 673−681.
(19) Zhan, Z.; Zheng, L.; Pan, Y.; Sun, G.; Li, L. *J. Mater. Chem.* **2012**, *22*, 2589−2595.
(20) Yang, Y.; Ren, L.; Zhang, C.; Huang, S.; Liu, T. *ACS Appl. Mater. Interfaces* **2011**, *3*, 2779−2785.
(21) Lerf, A.; He, H.; Forster, M.; Klinowski, J. *J. Phys. Chem. B* **1998**, *102*, 4477−4482.
(22) Guo, Y.; Wang, H.; He, C.; Qiu, L.; Cao, X. *Langmuir* **2009**, *25* (8), 4678−4684.
(23) Wu, J.; Shen, X.; Jiang, L.; Wang, K.; Chen, K. *Appl. Surf. Sci.* **2010**, *256*, 2826−2830.
(24) Graf, D.; Molitor, F.; Ensslin, K.; Stampfer, C.; Jungen, A.; Hierold, C.; Wirtz, L. *Nano Lett.* **2007**, *7* (2), 238−242.
(25) Ferrari, A. C.; Meyer, J. C.; Scardaci, V.; Casiraghi, C.; Lazzeri, M.; Mauri, F.; Piscanec, S.; Jiang, D.; Novoselov, K. S.; Roth, S.; Geim, A. K. *Phys. Rev. Lett.* **2006**, *97*, 187401(1−4).
(26) Eda, G.; Chhowalla, M. *Adv. Mater.* **2010**, *22*, 2392−2415.
(27) Rao, C. N. R.; Sood, A. K.; Subrahmanyam, K. S.; Govindaraj, A. *Angew. Chem., Int. Ed.* **2009**, *48*, 7752−7777.
(28) Swain, A. K.; Li, D.; Bahadur, D. *Carbon* **2013**, *57*, 346−356.
(29) Williams, G.; Kamat, P. V. *Langmuir* **2009**, *25* (24), 13869−13873.
(30) Singh, S.; Barick, K. C.; Bahadur, D. *CrystEngComm.* **2013**, *15*, 4631−4639.
(31) Yang, J.; Zhao, X.; Shan, X.; Fan, H.; Yang, L.; Zhang, Y.; Li, X. *J. Alloys Compd.* **2013**, *556*, 1−5.
(32) Zhan, Z.; Zheng, L.; Pan, Y.; Sun, G.; Li, L. *J. Mater. Chem.* **2012**, *22*, 2589−2595.
(33) Lv, T.; Pan, L.; Liu, X.; Sun, Z. *Catal. Sci. Technol.* **2012**, *2*, 2297−2301.

(34) Panigrahy, B.; Aslam, M.; Misra, D. S.; Ghosh, M.; Bahadur, D. *Adv. Funct. Mater.* **2010**, *20*, 1161−1165.
(35) Mukherjee, R.; Thomas, A. V.; Krishnamurthy, A.; Koratkar, N. *ACS Nano* **2012**, *6* (9), 7867−7878.
(36) Liu, Y. Z.; Li, Y. F.; Yang, Y. G.; Wen, Y. F.; Wang, M. Z. *Scripta Mater.* **2013**, *68*, 301−304.
(37) Li, C. C.; Du, Z. F.; Li, L. M.; Yu, H. C.; Wan, Q.; Wang, T. H. *Appl. Phys. Lett.* **2007**, *91*, 032101.
(38) Sing, K. S. W.; Everett, D. H.; Haul, R. .A. W.; Moscou, L.; Pierotti, R. A.; Rouquerol, J.; Siemieniewska, T. *J. Pure Appl. Chem.* **1985**, *57*, 603−619.
(39) Gopalakrishnan, K.; Govindaraj, A.; Rao, C. N. R. *J. Mater. Chem. A* **2013**, *1*, 7563−7565.
(40) Zhu, Y.; Murali, S.; Stoller, M. D.; Ganesh, K. J.; Cai, W.; Ferreira, P. J.; Pirkle, A.; Wallace, R. M.; Cychosz, K. A.; Thommes, M.; Su, D.; Stach, E. A.; Ruoff, R. S. *Science* **2011**, *332*, 1537−1541.
(41) Chen, S.; Zhu, J.; Wu, X.; Han, Q.; Wang, X. *ACS Nano* **2010**, *4*, 2822−2830.
(42) Yoo, J. J.; Balakrishnan, K.; Huang, J.; Meunier, M.; Sumpter, B. G.; Srivastava, A.; Conway, M.; Reddy, A. L. M.; Yu, J.; Vajtai, R.; Ajayan, P. M. *Nano Lett.* **2011**, *11* (4), 1423−1427.
(43) Wu, Q.; Xu, Y.; Yao, Z.; Liu, A.; Shi, G. *ACS Nano* **2010**, *4* (4), 1963−1970.
(44) Zhi, M.; Xiang, C.; Li, J.; Li, M.; Wu, N. *Nanoscale* **2013**, *5*, 72−88.
(45) Huang, Y.; Liang, J.; Chen, Y. *Small* **2012**, *8*, 1805−1834.
(46) Guo, H. L.; Wang, X. F.; Qian, Q. Y.; Wang, F. B.; Xia, X. H. *ACS Nano* **2009**, *3* (9), 2653−2659.
(47) Gao, W.; Singh, N.; Song, L.; Liu, Z.; Reddy, A. L. M.; Ci, L.; Vajtai, R.; Zhang, Q.; Wei, B.; Ajayan, P. M. *Nat. Nanotechnol.* **2011**, *6*, 496−500.
(48) Bei, F.; Hou, X.; Chang, S. L. Y.; Simon, G. P.; Li, D. *Chem.—Eur. J.* **2011**, *17*, 5958−5964.